Modern Physics Letters B
Vol. 36, No. 1 (2022) 2150499 (13 pages)

DOI: 10.1142/S0217984921504996

A highly sensitive D-type photonic crystal fiber infrared sensor with indium tin oxide based on surface plasmon resonance

Wei Liu[1,2,6], Chunjie Hu[3,7], Lei Zhou[4,8], Zao Yi[5,9], Ying Shi[1,2,10], Chao Liu[1,2,11], Jingwei Lv[1,2,12] and Lin Yang[1,2,13]

[1]*School of Physics and Electronic Engineering, Northeast Petroleum University, Daqing 163318, China*
[2]*Heilongjiang Provincial Cultivate Collaborative Innovation Center for Geothermal Resources Efficient Development and Comprehensive Utilization, Daqing 163318, China*
[3]*Department of Gynecology and Obstetrics, The Fourth Affiliated Hospital of Harbin Medical University, Harbin 150001, China*
[4]*Department of Orthopedics, The Second Affiliated Hospital of Harbin Medical University, Harbin 150081, China*
[5]*Joint Laboratory for Extreme Conditions Matter Properties, Southwest University of Science and Technology, Mianyang 621010, China*
[6]*1594813517@qq.com*
[7]*huchunjie2008@aliyun.com*
[8]*zhouleig4@aliyun.com*
[9]*yizaomy@swust.edu.cn*
[10]*shiyingdqpi@163.com*
[11]*msm-liu@126.com*
[12]*2009123@126.com*
[13]*583558294@qq.com*

Paul K. Chu

Department of Physics, Department of Materials Science and Engineering, and Department of Biomedical Engineering, City University of Hong Kong, Tat Chee Avenue, Kowloon, Hong Kong, China
paul.chu@cityu.edu.hk

Received 5 July 2021
Revised 23 August 2021
Accepted 23 August 2021
Published 15 December 2021

A highly sensitive surface plasmon resonance (SPR) sensor composed of a photonic crystal fiber (PCF) with the D-type structure is designed and analyzed by the full-vector finite element method (FEM). Indium tin oxide (ITO) is adopted as the plasmonic substance on account of the low cost and controllable infrared range (1500–2600 nm).

[11]Corresponding author.

By optimizing the structural parameters, the sensor shows a maximum wavelength sensitivity of 46,000 nm/RIU and average sensitivity of 13,166.67 nm/RIU for analyte refractive indexes between 1.355 and 1.385. This PCF combining a circular layout and D-type structure offers excellent sensitivity while the deposition and manufacturing complexity can be reduced. This sensor will possess an extremely expansive development space in the field of chemical analysis and environmental safety.

Keywords: PCF-SPR; indium tin oxide; high sensitivity; D-type sensing.

1. Introduction

Indium tin oxide (ITO) has become popular plasmonic material for surface plasmon resonance (SPR) sensing because of the low materials cost, controllable photoelectric properties, and small loss in the infrared range.[1,2] Compared to conventional plasmonic materials such as gold, silver, and aluminum,[3] ITO is a better conductor that can initiate surface plasmon polaritons (SPPs) in the visible region and even near-infrared regime.[2] In SPR excitation, the evanescent wave in total internal reflection (TIR) gives rise to collective oscillations of free electrons at the interface between the metal and dielectric. The vast majority of the energy of the incident light can be absorbed by the surface plasmon wave (SPW)[4,5] and the p-polarized light is coupled to the metal–dielectric interface when the phase matching condition is satisfied.[6–8] Therefore, there have been a crowd of efforts in designing SPR sensors with ITO for applications such as refractive index (RI) sensing, food safety,[9] chemical analysis,[10] biological detection,[11] and environmental monitoring.[12]

SPR has been implemented in multifarious types of sensing devices that incorporate prisms,[13] gratings,[14] conventional fibers,[15] and even photonic crystal fibers (PCFs). Among the various SPR sensing devices, PCF based on SPR sensors have attracted much interest to pave the way for single-mode transmission without compromising the high sensitivity in addition to the flexible multi-parameter functionality.[16–18] Recently, PCF-SPR sensors with ITO coatings have been proposed for RI sensing one after another. For instance, Dash *et al.*[19] have demonstrated an SPR biosensor based on PCF with an ITO coating on the air holes for liquid sensing and the sensor shows a sensitivity of 2000 nm/RIU and resolution of 5×10^{-5} RIU in the wavelength range of 1400–1600 nm. Liu *et al.*[20] have investigated the rectangular-grid PCF-SPR sensor coated with ITO on the outside of the cladding and it has a maximum sensitivity of 35,000 nm/RIU in the wavelength range from 1380 nm to 2260 nm. Rahman *et al.*[21] have presented a PCF-SPR sensor with an irregular hexagonal core and ITO as the conductive layer and it shows a spectral sensitivity of 37,000 nm/RIU and resolution of 2×10^{-5} RIU in the range from 1470 nm to 2220 nm. Nevertheless, the operating wavelength of these sensors is limited to about 2200 nm and the spectral sensitivity is still not satisfactory. Furthermore, the coatings are typically deposited onto the internal air holes or external cladding and the complex manufacturing process and high cost are not satisfactory.

Herein, a D-type PCF-SPR sensor with the ITO coating is designed to improve the sensitivity in the infrared region (1500–2600 nm). With the side surface

polished, a flat plane is formed to fabricate the D-type PCF and deposition can be performed more easily and uniformly boding well for commercial adoption. In this case, the ITO films can be deposited precisely to better excite SPR for RI sensing. By optimizing the structural parameters, such as the size, distance, species of the air holes, as well as the thickness, width, and length of the ITO films, the sensor shows an average sensitivity of 13,166.67 nm/RIU, maximum wavelength sensitivity of 46,000 nm/RIU, and high resolution of 2.17×10^{-6} RIU for analyte RIs between 1.355 and 1.385.

2. Structural Design and Numerical Modeling

Figure 1(a) describes the cross-section of the D-type PCF-SPR sensor. Compared to the traditional full-circular structure, the coating platform is not only reduced, but also the distance between the metal films and the fiber core is shortened by side polishing technology. Thus, the phase matching between the core mode and surface plasmon polariton (SPP) mode can be further improved. Fused silica is selected as the background materials and ITO is the plasmonic materials. The effective RI of the cladding can be reduced by filling a series of air holes in the PCF. The designed

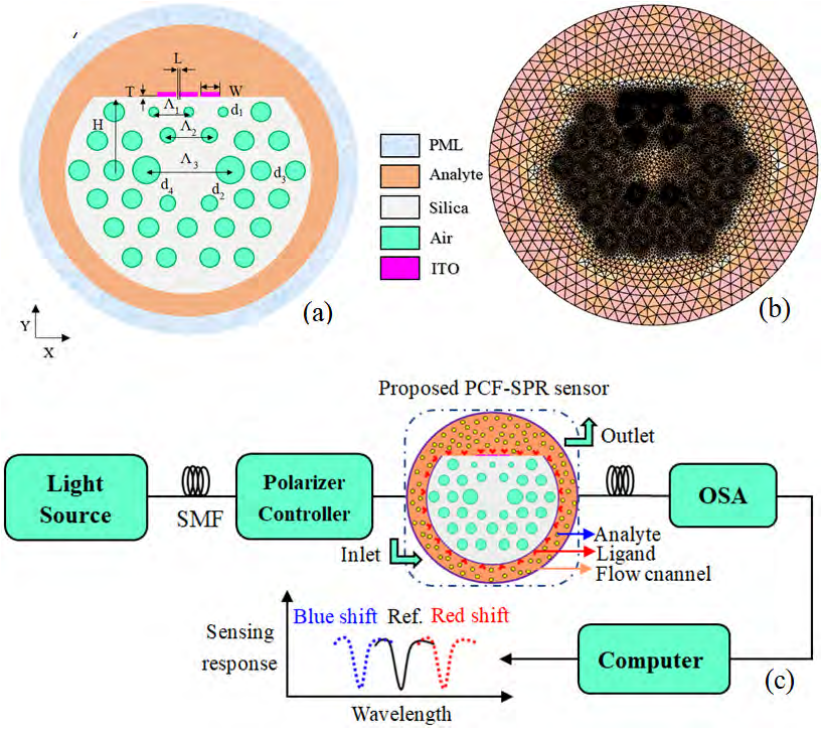

Fig. 1. (Color online) (a) Cross-sectional of the sensor, (b) Grid division in the model, and (c) Experimental setup for the PCF-SPR RI sensor.

PCF is a step type optical fiber, which is beneficial to constrain the transmission of incident light in the fiber core to reduce transmission loss. Based on the light guiding mechanism of total internal reflection (TIR), the incident light transmits in the PCF and supports the evanescent field to excite SPR. Recently, the manufacturing technology and surface coating technology of PCF have been gradually improved and developed rapidly. The PCF can be fabricated by the standard stack and draw method.[11] In this method, many fine capillaries are stacked and inserted into the glass tube corresponding to outer cladding to obtain a fiber perform, and then the fiber perform is drawn into PCF. In fiber drawing process, a pressure is applied to maintain air holes and the air hole diameter also can be controlled. To obtain uniformed ITO layer on the D-type region, chemical vapor deposition (CVD) technique can be employed to offer minimal surface roughness.[22] By optimizing the different structural parameters, the size of the different air holes (d_1 to d_4) are determined to be 0.5, 1.0, 1.3 and 1.6 μm and the pitches of the air holes (Λ_1, Λ_2, Λ_3) are 2.0, 2.3 and 4.4 μm, respectively. The D-type platform from the center (H) is 4.5 μm and the thickness (T), width (W), and length (L) of the ITO film are 70 nm, 0.95 μm and 0.3 μm, respectively. The permittivity of ITO is calculated by the following equation[19]:

$$\varepsilon(\omega) = \varepsilon - \frac{\omega_p^2}{\omega^2 + i\omega\Gamma}, \tag{1}$$

where ε is the intraband dielectric constant, Γ is the damping coefficient, $\omega_p^2 = ne^2/\mu\varepsilon_0$, $\mu = 0.3$ m_e, $\omega_p = 2.19$ eV and $\Gamma = 0.111$ eV. The effective RI of fused silica can be determined by Sellmeier's equation[23]

$$n^2 - 1 = \frac{A_1\lambda^2}{\lambda^2 - B_1^2} + \frac{A_2\lambda^2}{\lambda^2 - B_2^2} + \frac{A_3\lambda^2}{\lambda^2 - B_3^2}, \tag{2}$$

where n is the effective RI and λ stands for the wavelength. The Sellmeier's constants are $A_1 = 0.6961663$, $A_2 = 0.4079426$, $A_3 = 0.8974790$, $B_1 = 0.0684043$ μm, $B_2 = 0.1162414$ μm and $B_3 = 9.8961610$ μm.

The full-vector finite element method (FEM) is implemented in the numerical analysis. A perfectly matched layer (PML) is considered as the boundary condition to absorb the transitory field dispersed from the PCF structure.[24,25] The confinement loss (CL) of the core mode is frequently used to evaluate the SPR properties and determined by Eq. (3)[26]

$$\alpha_L(\text{dB/cm}) = 8.686 \times \frac{2\pi}{\lambda}\text{Im}[n_{\text{eff}}] \times 10^4, \tag{3}$$

where λ stands for the operating wavelength in micrometers and $\text{Im}[n_{\text{eff}}]$ refers to the imaginary part of the effective RI.

Convergence tests are carried out by optimizing the mesh size and PML thickness so as to produce more accurate results. The computational area is meshed with triangular domain elements (41,612), boundary domain elements (1893), as well as

minimum unit quality (0.5432) displayed in Fig. 1(b). The experimental setup described in Fig. 1(c) can be used to demonstrate the practicality of the PCF-SPR sensor. In the measurement, a beam of light from a laser impinges the single-mode fiber (SMF) through a polarization controller. The RI sensor with the ITO coating is placed in the reaction vessel so that it contacts the analyte adequately. On the surface of the ITO films, flow cells exist. The biomolecules in the sample (analyte) having different RIs interact with the ligand causing shifts (blueshift or redshift) in the resonance wavelength through optical spectrum analyzer (OSA) and the results are analyzed by a computer.

3. Results and Discussion

The CL spectra and energy distribution of the light field in Fig. 2(a) show that CL of the x and y-polarized modes increases first and then decreases with the wavelength increasing. However, the CL peak of the y-polarized mode is higher and sharper than that of the x-polarized mode. The two large air holes on both sides of the fiber core make the area of the longitudinal (y) mode field larger than that of the transverse (x) mode field. Owing to the polarization effect, the y-polarized mode demonstrates a larger evanescent field resulting in stronger coupling with the ITO films than the x-polarized mode as shown in Fig. 2(a) insets. Hence, the y-polarized mode is taken into account in the analysis. Figure 2(b) shows the CL spectra (red) and dispersion relationship of the core mode (blue) and SPP mode (black) for an ITO thickness (T) of 70 nm, width (W) of 0.95 μm, and length (L) of 0.30 μm. When Re(n_{eff}) of the core mode is equal to that of the SPP mode, there occurs a resonant coupling between the two modes. Furthermore, phase matching conditions can be observed at 2150 nm for an analyte RI of 1.355. Inset in Fig. 2(b) shows the core mode and sharp CL peak due to stronger resonance effects between the core and SPP modes.

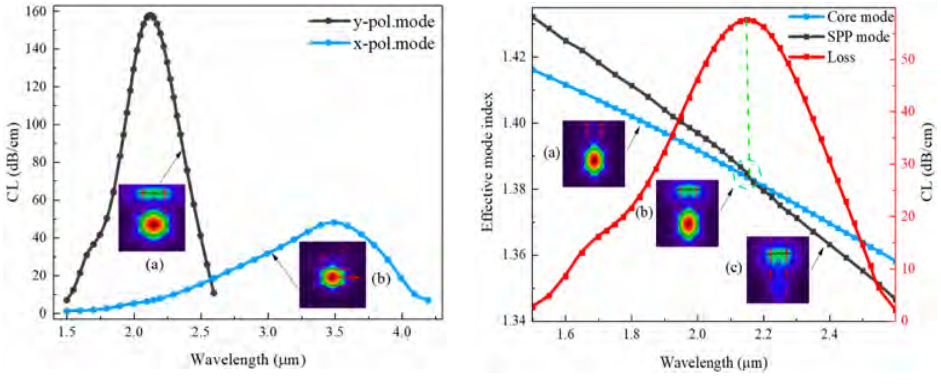

(a) (b)

Fig. 2. (Color online) (a) Variation of CL spectra of the x-polarized and y-polarized modes and (b) dispersion relationship of the core mode, SPP mode and CL spectrum.

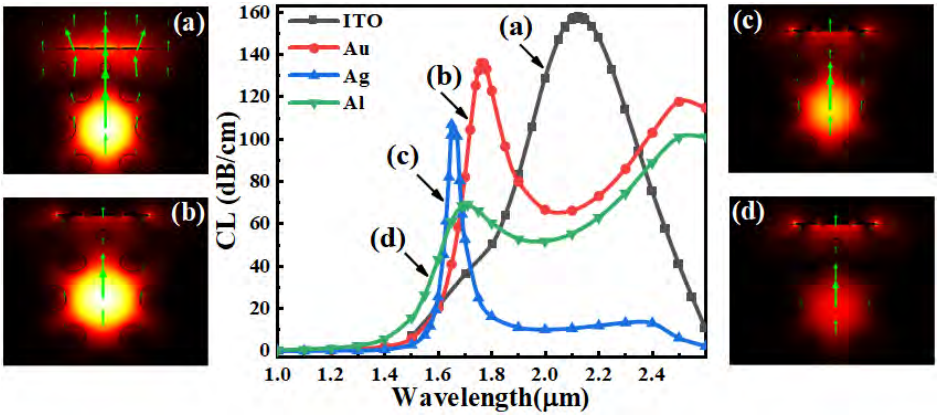

Fig. 3. (Color online) CL spectra of different kinds of plasmonic films and light field distributions for the corresponding resonant wavelengths.

The choice of the plasmonic materials plays a crucial role in the performance of the PCF-SPR sensor and gold, silver and aluminum are popular. However, since metal thin films are easily oxidized in solutions, oxides such as ITO have attracted a great deal of attention. Figure 3 compares the CL spectra and energy distributions of the light field of gold, silver, aluminum and ITO for $n = 1.355$ and $T = 70$ nm. The loss peak decreases gradually from ITO to aluminum. The loss peak of ITO is the largest and there is more energy transferred from the fiber core to ITO film as shown in Fig. 3(a) in comparison with Figs. 3(b)–3(d). Hence, stronger resonant effects and better mode coupling are accomplished. Besides, the resonance wavelength decreases gradually from ITO to aluminum showing a blueshift. In comparison with traditional metals, ITO has a broader application prospects.

The properties of the PCF-SPR sensor are optimized by changing the structural parameters. The arrangement of air holes has a crucial effect on the energy of the core mode and the sizes of air holes influence coupling and phase matching. Figure 4(a) shows the variations of the CL spectra with air holes d_1. CL is almost the same at the resonant wavelength of 1.8 μm when d_1 becomes larger (0.30–0.50 μm). Taking 1.8 μm as the separation point, CL on the left decreases but increases on the right, and so the optimal d_1 is 0.5 μm. The dependence of the CL spectra on the air hole size d_2 is presented in Fig. 4(b). Compared to the variations with d_1, the resonance peaks become higher and sharper with decreasing d_2 suggesting stronger resonance effects between the core mode and SPP mode at 1.0 μm. In addition, the smaller diameter of air holes d_2 provides a wider channel, which is helpful to transfer the energy inside the fiber core to the metal surface. Therefore, the different sizes and positions of the air holes in the cladding not only effectively restrain most of the incident light in the fiber core, but also allow the light to reach the surface of ITO films through the gap of the small air holes (d_1 and d_2), further realizing efficient sensing.

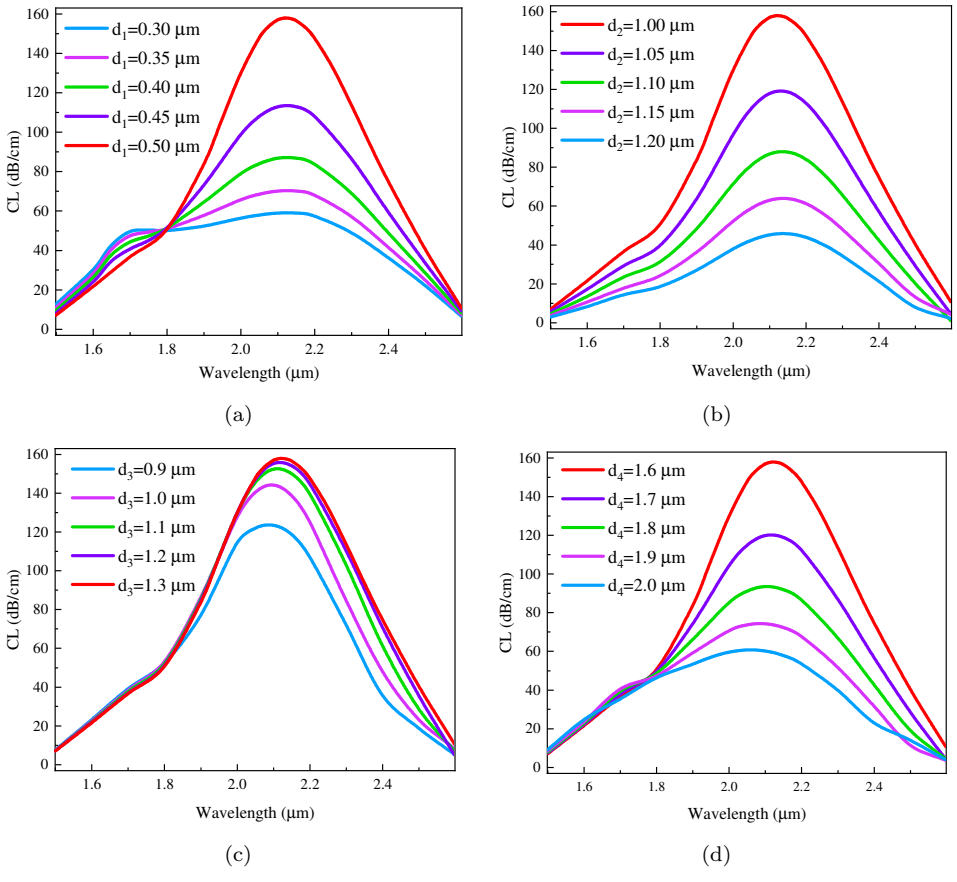

Fig. 4. (Color online) CL spectra of the sensors with different air holes. (a) d_1, (b) d_2, (c) d_3 and (d) d_4.

Figure 4(c) shows the CL spectra for different diameters of air holes d_3. As d_3 increases, the peak increases gradually, but when d_3 is more than 1.1 μm, the variable quantity of the resonance peak decreases, indicating that when d_3 is too large, coupling between the two modes is almost unchanged. The influence of the diameter of the air hole d_4 on the CL spectra is shown in Fig. 4(d). When d_4 increases (1.6–2.0 μm), the resonant peak decreases gradually and becomes less sharp, indicating that smaller diameter of air holes (d_4) provides a larger light field area and allows more energy to be confined in the fiber core. Furthermore, there are more photons interacting with free electrons at the interface between the ITO films and dielectrics to produce better resonance effects.[1,20]

The influence of the pitches of the air holes on the sensing properties is shown in Fig. 5. CL decreases as Λ_1 increases as shown in Fig. 5(a) because a smaller Λ_1 constrains propagation of light to better meet the phase matching conditions. Compared to the variations of Λ_1, the resonance effect is more pronounced and the

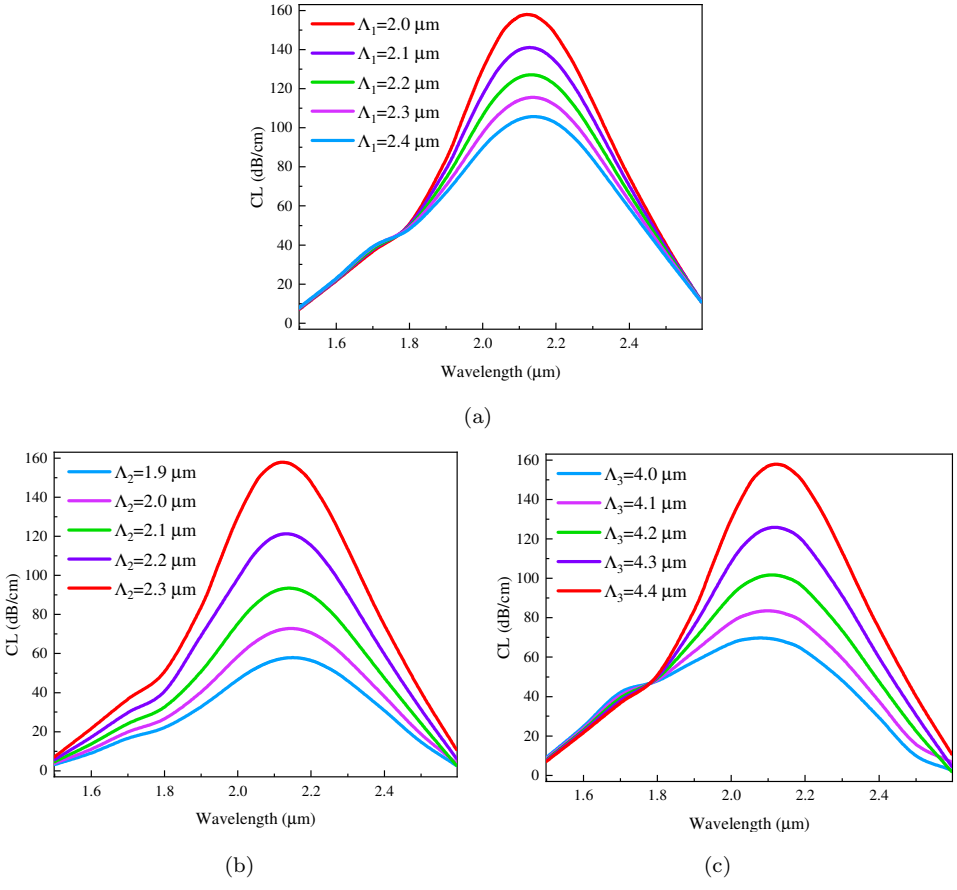

Fig. 5. (Color online) CL spectra for different air hole pitches. (a) Λ_1, (b) Λ_2 and (c) Λ_3.

resonance peaks become higher and sharper with decreasing Λ_2 and Λ_3. This can be explained that if the air hole space near the fiber core becomes larger, more energy fills the fiber core consequently facilitating energy transmission to the metal surface. Therefore, the optimal air hole pitches are $\Lambda_1 = 2.0$ μm, $\Lambda_2 = 2.3$ μm and $\Lambda_3 = 4.4$ μm.

Figures 6(a)–6(c) show the CL spectra for different ITO thickness (T), width (W) and length (L), respectively. The excellent performance of the PCF-SPR sensor stems from the superior plasmonic materials. The thickness (T) plays a key role in the CL and sensitivity. Figure 6(a) shows the effects of the ITO film thickness on the CL spectra for an analyte RI of 1.355. On the one hand, the resonant wavelength displays a redshift with T from 65 nm to 85 nm. It is attributed to the Re(n_{eff}) of the fundamental mode which is nearly unchanged, while the Re(n_{eff}) of SPP mode increases. On the other hand, the CL peak decreases indicating that less energy is transferred between the two modes. When the ITO film thickness is 65 nm, the loss peak is the largest and for better sensing sensitivity, the optimal ITO film

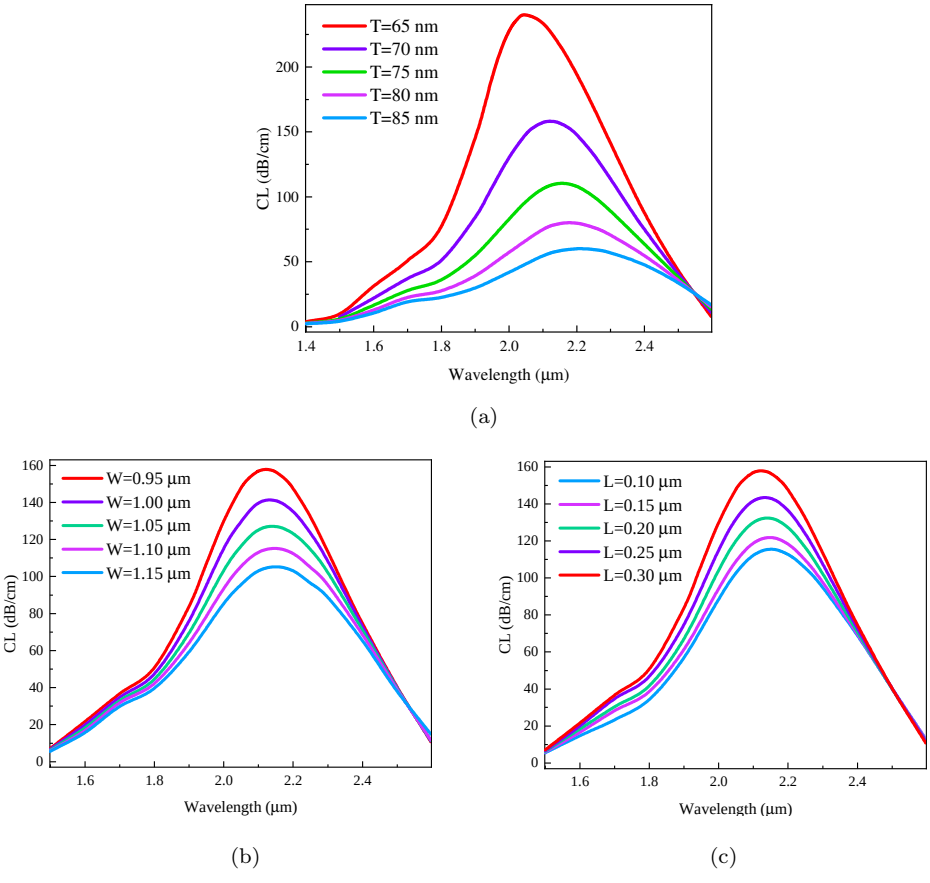

Fig. 6. (Color online) CL spectra of the sensor with different ITO parameters. (a) Thickness (T), (b) width (W) and (c) length (L).

thickness T is chosen to be 70 nm. When the width (W) changes between 0.95 and 1.15 μm, the CL peak declines and tends to be flat as shown in Fig. 6(b). In addition, Fig. 6(c) illustrates that there is a small blueshift when the ITO length (L) changes from 0.10 μm to 0.30 μm. It is indicated that the Re(n_{eff}) of SPP mode decreases, while the Re(n_{eff}) of fundamental mode is invariable, and the loss peak increases significantly. Therefore, more energy is transferred from the fiber core to the surface of the ITO films to boost resonance when the excited SPP mode matches the core mode.

The height (H) is another vital parameter of the D-type sensor and the CL spectra for different heights from 4.5 μm to 4.9 μm are presented in Fig. 7. The loss spectra become smoother when the height increases indicating that the further away the ITO film is from the fiber core, the worse are the coupling effects of the two modes. Therefore, it is more difficult to achieve phase matching to produce the desirable resonance effects.

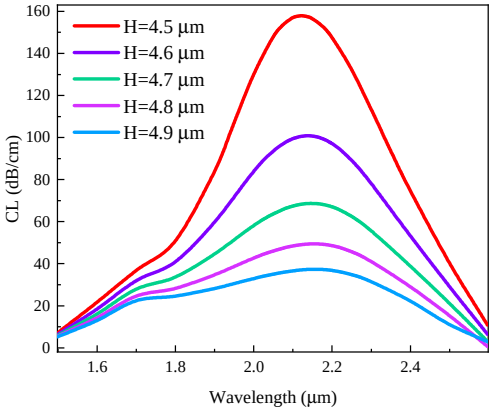

Fig. 7. (Color online) CL spectra of the sensor for different heights (H) from 4.5 μm to 4.9 μm.

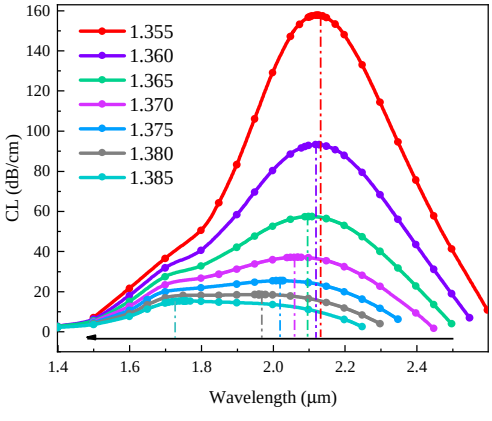

Fig. 8. (Color online) CL spectra for different analyte RIs from 1.355 to 1.385.

SPR is sensitive to tiny variations in the RI of the surrounding analyte. When the analyte RIs change, the phase matching point exhibits either blueshift or redshift. Figure 8 shows that as the analyte RIs change from 1.355 to 1.385, the resonance wavelength moves in the direction of the origin of the coordinates. For an analyte RI of 1.355, more energy is transferred from the fiber core to the surface of ITO films and two modes realize the best phase matching. In general, the effectiveness of the PCF-SPR RI sensor can be gauged by the wavelength sensitivity (WS) as shown in the following[27]:

$$S(\mathrm{nm/RIU}) = \frac{\Delta\lambda_{\mathrm{peak}}}{\Delta n_a}, \tag{4}$$

where Δn_a refers to the variation of two successive analyte RIs and $\Delta\lambda_{\mathrm{peak}}$ denotes the difference in the peak wavelength shift due to changes in the analyte RIs.

For analytes RIs varying from 1.355 to 1.385 ($\Delta n_a = 0.005$), the resonance peaks appear at 2125, 2120, 2100, 2070, 2025, 1960 and 1730 nm, respectively. The resonance wavelengths shift from 1960 to 1730 nm (230 nm), which is the maximum as the analyte RIs increase from 1.38 to 1.385. It leads to a maximum wavelength sensitivity of 46,000 nm/RIU and average sensitivity of 13,166.67 nm/RIU.

The resolution is also key performance index which reflects the ability to detect minute variations in the analyte RIs. The resolution is calculated by the following equation[28]:

$$R(\text{RIU}) = \Delta n_a \frac{\Delta\lambda_{\min}}{\Delta\lambda_{\text{peak}}}, \tag{5}$$

where Δn_a is the change in the analyte RIs, $\Delta\lambda_{\min}$ is the minimum spectral resolution, and the maximum resonant wavelength peak shift is defined by $\Delta\lambda_{\text{peak}}$. For $\Delta n_a = 0.005$, $\Delta\lambda_{\min} = 0.1$ and $\Delta\lambda_{\text{peak}} = 230$ nm. Therefore, a maximum resolution of 2.17×10^{-6} RIU can be obtained and the characteristics of the sensor for different analyte RIs are summarized in Table 1. Figure 9(a) shows the correlation between the resonance wavelength and RIs and the polynomial fit in Fig. 9(b) shows R^2 of 0.9869 suggesting good linearity.

Table 1. Characteristics of the sensor for different analyte RIs.

Analyte RI	CL (dB/cm)	Res. wavelength (nm)	Peak shift (nm)	Sensitivity (nm/RIU)	Resolution (RIU)
1.355	157.80	2125	5	1000	1.00×10^{-4}
1.360	93.04	2120	20	4000	2.50×10^{-5}
1.365	57.06	2100	30	6000	1.67×10^{-5}
1.370	36.75	2070	45	9000	1.11×10^{-5}
1.375	25.01	2025	65	13000	7.69×10^{-6}
1.380	18.07	1960	230	46000	2.17×10^{-6}
1.385	14.68	1730	N/A	N/A	N/A

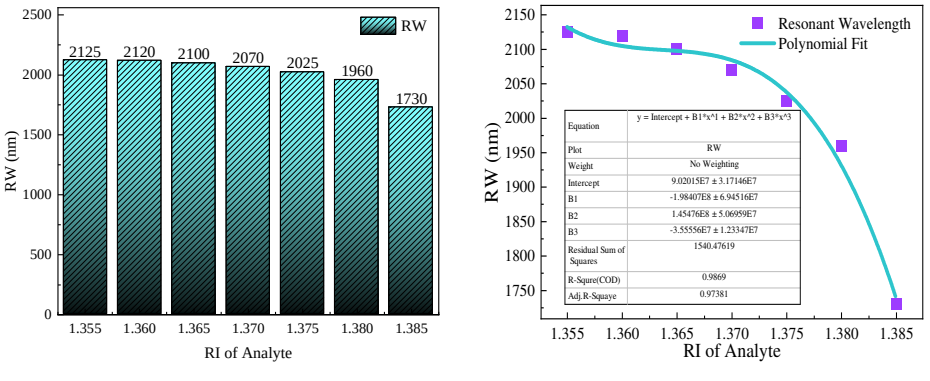

(a) (b)

Fig. 9. (Color online) (a) Histograms showing the resonance wavelengths for different analyte RIs and (b) polynomial fit of analyte RIs.

4. Conclusion

A PCF-SPR sensor with ITO coatings that can be operated in the infrared region (1500–2600 nm) is designed and analyzed. The structure is optimized by constantly adjusting the structural parameters with the wavelength interrogation technique. An average sensitivity of 13,166.67 nm/RIU, maximum wavelength sensitivity of 46,000 nm/RIU, and high resolution of 2.17×10^{-6} RIU are achieved for analyte RIs between 1.355 and 1.385. Owing to the simple structure, fabrication of the sensor is straightforward by existing techniques. The excellent properties of the sensor suggest large potential in accurate and precise detection in the chemical and environmental safety fields.

Acknowledgments

This work was jointly supported by the Local Universities Reformation and Development Personnel Training Supporting Project from Central Authorities (No. 140119001), City University of Hong Kong Strategic Research Grant (SRG) (No. 7005505), and Scientific Research Fund of Sichuan Province Science and Technology Department (No. 2020YJ0137).

References

1. C. Liu *et al.*, *Opt. Commun.* **464** (2020) 125496.
2. S. Franzen, *J. Phys. Chem. C* **112** (2008) 6027.
3. A. A. Noman *et al.*, *Sensors* **20** (2020) 6049.
4. M. H. Salman, H. K. Muhammad and H. A. Yasser, *Period. Eng. Nat. Sci.* **8**(3) (2020) 1288.
5. W. Liu *et al.*, *Results Opt.* **1** (2020) 100004.
6. M. De *et al.*, *Plasmonics* **15** (2020) 1429.
7. A. Gupta*et al.*, *Plasmonics* **15** (2020) 1323.
8. A. A. Rifat *et al.*, *IEEE Photon. J.* **8**(1) (2016) 4800408.
9. M. Liu *et al.*, *Mod. Phys. Lett. B* **31**(36) (2017) 1750352.
10. A. A. Rifat *et al.*, *IEEE Sens. J.* **17**(9) (2017) 2776.
11. F. Haider *et al.*, *J. Opt. Soc. Am. B* **35**(11) (2018) 2816.
12. J. W. Wang *et al.*, *Results Phys.* **18** (2020) 103240.
13. J. N. Dash and R. Jha, *Plasmonics* **11**(6) (2016) 1505.
14. A. Patnaik, K. Senthilnathan and R. Jha, *IEEE Photon. Tech. Lett.* **27**(23) (2015) 2437.
15. C. Liu *et al.*, *Opt. Commun.* **382** (2017) 162.
16. W. Liu *et al.*, *Opt. Exp.* **29**(25) (2021) 40734.
17. X. Zhou *et al.*, *OSA Contin.* **1**(4) (2018) 1332.
18. S. H. Zhang *et al.*, *Appl. Phys.* **46** (2018) 311.
19. J. N. Dash and R. Jha, *IEEE Photon. Tech. Lett.* **26**(6) (2014) 595.
20. Q. Liu *et al.*, *Opt. Mater.* **120** (2020) 109800.
21. K. M. M. Rahmana *et al.*, *Results Phys.* **23** (2021) 103983.
22. N. Sakib *et al.*, *Opt. Mater. Exp.* **11**(2) (2021) 273.
23. S. X. Jiao, S. F. Gu, H. R. Fang and H. R. Yang, *Plasmonics* **14** (2019) 685.

24. M. R. Islam *et al.*, *Opt. Quantum Electron.* **53** (2021) 112.
25. S. A. Mitu *et al.*, *Opt. Laser Eng.* **140**(18) (2021) 106551.
26. S. Singh and Y. K. Prajapati, *Appl. Phys.* **125**(6) (2019) 437.
27. H. X. Han *et al.*, *Sensors* **20**(14) (2019) 3911.
28. A. A. Rifat *et al.*, *Opt. Exp.* **24**(3) (2016) 2485.